AIMS Energy

AIMS Energy, 14(3): 602–617.
DOI: 10.3934/energy.2026025
Received: 01 April 2026
Revised: 15 May 2026
Accepted: 22 May 2026
Published: 26 May 2026

http://www.aimspress.com/journal/energy

Research article

Electronic modulation in a defect-rich high-entropy NiCoFeCu LDH enables accelerated oxygen evolution

Chengshuo Du, Shuxing Bai* and Mingrui Guo*

College of Chemistry and Chemical Engineering, Qingdao University, Qingdao 266071, Shandong, P. R. China

* **Correspondence:** Email: shuxbai@qdu.edu.cn, gmrqddx@qdu.edu.cn.

Abstract: Accelerating the oxygen evolution reaction (OER) is critical for efficient alkaline water electrolysis in green hydrogen production. Rational regulation of the electronic structure of transition metal (oxy)hydroxides offers a vital route to enhance their OER kinetics under alkaline conditions. Herein, we reported a defect-rich high-entropy layered double hydroxide, D-NiCoFeCu-LDH, constructed via a sequential electrodeposition–electrochemical etching strategy. Selective chromium leaching reconstructs a homogeneous Ni–Co–Fe–Cu high-entropy matrix while introducing abundant vacancies and lattice distortion. Structural characterization confirms uniform elemental distribution and defect-enriched nanosheet arrays, whereas X-ray photoelectron spectroscopy (XPS) analysis reveals pronounced electronic redistribution, manifested by increased high-valence Ni^{3+}/Co^{3+} species and positive binding energy shifts. We proposed that highly dispersed Cu^{+}/Cu^{2+} species act as electronic modulators, withdrawing electron density from neighboring Ni, Co, and Fe centers, while lattice distortion further promotes electronic reconfiguration. Electrochemical measurements demonstrated enhanced intrinsic activity and accelerated charge-transfer kinetics compared to quaternary counterparts. Importantly, in situ attenuated total reflection surface-enhanced infrared absorption spectroscopy (ATR-SEIRAS) directly verified facilitated *OOH intermediate formation at lower overpotential, establishing a molecular-level link between electronic modulation and improved OER kinetics. In this work, we provide mechanistic insight into how synergistic high-entropy regulation and defect engineering cooperatively enhance intrinsic catalytic activity, offering a framework for designing durable, high-performance OER electrocatalysts.

Keywords: high-entropy materials; layered double hydroxide; electronic structure modulation; defect engineering; oxygen evolution reaction

1. Introduction

The shift toward a sustainable energy future hinges on the large-scale production of green hydrogen via alkaline water electrolysis, a technology poised to play a central role in the global decarbonization effort [1]. However, its widespread deployment is severely hampered by the oxygen evolution reaction (OER), a kinetically sluggish half-reaction that imposes a major overpotential penalty and limits overall energy conversion efficiency [2]. Although Ni-, Co-, and Fe-based (oxy)hydroxides rank among the most promising earth-abundant OER catalysts, their intrinsic activity and structural stability remain inadequate under industrially relevant current densities, hindering practical implementation [3]. Therefore, developing catalyst architectures that simultaneously boost activity and durability has become a pressing priority in the field of energy electrocatalysis.

Electronic structure modulation of catalytically active metal centers has emerged as a powerful approach to improving OER performance. Incorporation of secondary metal elements can regulate the adsorption energetics of key OER intermediates (*OH, *O, *OOH) by tuning the electronic configuration and metal–oxygen bonding characteristics of transition metal sites [4–6]. Among dopants, copper is particularly attractive due to its relatively high electronegativity and accessible multivalent states, which enable it to influence local electron density and interfacial charge redistribution in multi-metal systems [7,8]. However, in conventional multicomponent hydroxides, compositional inhomogeneity and phase segregation often limit the uniformity of electronic interactions, thereby restricting the extent of cooperative catalytic enhancement.

High-entropy materials (HEMs) provide an alternative design paradigm to address these challenges. By incorporating principal elements in near-equimolar proportions, HEMs maximize configurational entropy, which thermodynamically stabilizes homogeneous solid solutions and suppresses phase segregation [9]. The resulting intrinsic lattice distortion and chemical disorder can introduce lattice strain and facilitate electronic redistribution, potentially optimizing intermediate adsorption and reaction kinetics [10]. However, the rational integration of high-entropy design with precise defect engineering in LDHs, along with a clear mechanistic understanding of their synergy during OER, is lacking.

Herein, we report a defect-rich multi-metal high-entropy layered double hydroxide (D-NiCoFeCu-LDH) constructed via a rational "electrodeposition–electrochemical etching" strategy. A NiCoFeCuCr-LDH precursor is first electrodeposited on nickel foam, followed by selective electrochemical leaching of chromium through cyclic voltammetry (CV). This process serves dual functions: (i) Reconstructing a stable high-entropy Ni–Co–Fe–Cu matrix with homogeneous elemental distribution, and (ii) deliberately introducing abundant vacancies and lattice distortion through controlled etching. We propose that the cooperative high-entropy/defect environment, together with highly dispersed Cu species, induces pronounced electronic modulation of neighboring Ni, Co, and Fe active centers, thereby enhancing their intrinsic OER activity. Through comprehensive structural characterization (SEM, TEM, XRD, XPS), systematic electrochemical evaluation, and operando in situ ATR-SEIRAS analysis, we establish a coherent structure–electronic structure–activity–mechanism relationship. In this work, we demonstrate that coupling high-entropy stabilization with precise defect engineering offers a rational and potentially generalizable strategy for designing high-performance and durable OER electrocatalysts.

2. Materials and methods

2.1. Materials

Nickel(II) nitrate hexahydrate ($Ni(NO_3)_2·6H_2O$, 99.9%), cobalt(II) nitrate hexahydrate ($Co(NO_3)_2·6H_2O$, ≥99%), copper(II) nitrate trihydrate ($Cu(NO_3)_2·3H_2O$, ≥99%), chromium(III) nitrate nonahydrate ($Cr(NO_3)_3·9H_2O$, ≥99%), ferrous sulfate ($FeSO_4$, ≥99%), and potassium hydroxide (KOH, 95%) were purchased from Sinopharm Chemical Reagent Co., Ltd. Nickel foam was obtained from Kunshan Guangjiayuan New Materials Co., Ltd. Deionized water used in the experiments was prepared by a laboratory water purification system. All reagents were used as received without further purification.

2.2. Methods

Nickel foam (NF, 1 cm × 2 cm) was sequentially cleaned with 1 M HCl, distilled water, and anhydrous ethanol for 15 min each, then vacuum-dried at 60 ℃. FeCoNiCuCr-LDH/NF was synthesized by potentiostatic electrodeposition. NF, a graphite rod, and an Ag/AgCl electrode served as the working, counter, and reference electrodes, respectively. Electrodeposition was carried out on a CHI 760E workstation at −1.0 V for 600 s. The electrolyte consisted of 0.24 M $Ni(NO_3)_2·6H_2O$, 0.24 M $Co(NO_3)_2·6H_2O$, 0.05 M $Cu(NO_3)_2·3H_2O$, 0.015 M $Cr(NO_3)_3·9H_2O$, and 0.06 M $Fe(NO_3)_3·9H_2O$. Electrochemical activation of FeCoNiCuCr-LDH/NF was performed in 1.0 M KOH using the sample as the working electrode, a 1 cm × 1 cm platinum sheet as the counter electrode, and a saturated Hg/HgO electrode as the reference. CV was conducted for 200 cycles between 1.0 and 1.5 V at 50 mV s^{-1}. For comparison, D-FeCoNi-LDH/NF, D-FeCoCu-LDH/NF, D-FeNiCu-LDH/NF, and D-CoNiCu-LDH/NF were prepared under identical conditions.

2.3. Material characterization

Using a scanning electron microscope (SEM) (Thermo scientific Apreo 2C, energy spectrum OXFORD ULTIM Max65) and transmission electron microscope (Thermo Scientific TF20, USA), the morphology of the material was characterized by an energy spectrometer (EDAX) and a high-resolution electron microscope (JEM-F200). The microstructure and phase of the samples were analyzed by X-ray diffractometer (SmartLab, CuKα radiation). The surface/internal characteristics of the samples were established using ESCALAB QXI XPS. The material was subjected to electron paramagnetic resonance (EPR) testing using Bruker EMX Plus to characterize the changes in oxygen vacancies.

2.4. Electrochemical testing

The electrocatalytic performance was evaluated on a CHI 760E electrochemical workstation using a standard three-electrode system. The as-prepared catalyst on NF was directly used as the working electrode, with a 1 cm × 1 cm platinum sheet as the counter electrode and a saturated Hg/HgO electrode as the reference. Measurements were carried out in 1.0 M KOH. Linear sweep voltammetry (LSV) was recorded with 85% iR compensation. Tafel slopes were obtained by fitting the linear region of the polarization curves to the Tafel equation: $\eta = b \log |j| + a$. Electrochemical impedance spectroscopy (EIS) was performed at the selected overpotential over a frequency range of 1 kHz to 10 Hz with an AC amplitude of 5 mV. The electrochemical active surface area (ECSA) was determined by CV in a small potential range at different scan rates. The scan frequencies of the CV were 2, 4, 6, 8, and 10 $mV \cdot s^{-1}$.

3. Results and discussion

3.1. Representation

To achieve precise control over multi-active site synergism and structural defects, we designed and synthesized a defect-rich multi-metallic high-entropy layered double hydroxide (D-NiCoFeCu-LDH). As shown in Figure 1a, we first grew the NiCoFeCuCr-LDH precursor on a nickel foam (NF) substrate using a controlled electrodeposition method. The chromium element was then selectively leached via CV, leading to the reconstruction of D-NiCoFeCu-LDH, rich in defects. This “synthesis-etching” strategy successfully introduced abundant vacancies and lattice distortions while effectively modulating the material’s electronic structure and surface-active site distribution. To gain further insight into the synthesized material, we performed a series of morphological and structural characterizations. SEM images (Figure 1b) showed that D-NiCoFeCu-LDH was uniformly grown as vertically aligned nanosheet arrays on the 3D nickel foam framework, forming an open and interconnected porous network structure. The size distribution of the nanosheets (Figure 2) revealed a uniform diameter centered around 0.606 nm. This 3D porous architecture was beneficial for exposing more active sites and promoting electrolyte penetration and product gas diffusion. Transmission electron microscopy (TEM) images (Figure 1c) further confirmed the ultrathin and wrinkled morphology of the nanosheets, which significantly increased the material’s surface area. High-resolution TEM (HRTEM) images (Figure 1d) showed lattice fringes approximately 0.230 nm and 0.202 nm, corresponding to the (015) plane of $Ni(OH)_2$ and the (200) crystal plane of NiO, respectively. Due to the relatively low crystallinity of the material and its sensitivity to electron beams, part of the $Ni(OH)_2$ may have transformed into NiO during imaging, a phenomenon consistent with the electron beam sensitivity of low-crystallinity hydroxides, as reported in the literature [11]. The selected area electron diffraction (SAED) pattern in Figure 1c exhibits diffuse halo rings, indicating low overall crystallinity and abundant defect structures. Recognizable lattice spacings of approximately 0.76 nm were partly consistent with the (001) plane of $Ni(OH)_2$, albeit with weak intensity, further demonstrating poor long-range order. This result indirectly indicates the presence of rich lattice distortions and defect structures at the atomic scale.

To elucidate the distribution of multi-metallic elements, we conducted element mapping analysis (Figure 1e). The results showed a highly uniform distribution of Fe, Co, Ni, Cu, and O within the nanosheets, with no apparent phase segregation. This uniform elemental mixing is a characteristic feature of high-entropy materials, with atomic percentages of each component ranging from 5 to 35 at.%, in line with the thermodynamic definition of a high-entropy system [12]. Energy-dispersive X-ray spectroscopy (EDS) quantitative analysis (Table 1) further confirmed the successful synthesis of a multi-element LDH material with high configurational entropy, with atomic percentages of Fe, Co, Ni, and Cu at 13 at.%, 26 at.%, 22 at.%, and 18 at.%, respectively. Inductively coupled plasma atomic emission spectroscopy (ICP-OES) quantitative analysis (Table 2) further verified the elemental composition of the catalyst. The atomic percentages of Fe, Co, Ni, Cu, and Cr in D-FeCoNiCu-LDH/NF were 16.13%, 32.3%, 27.3%, 22.33%, and 1.6%, respectively. For comparative studies, we synthesized four additional four-metal defect-rich LDHs (D-NiFeCu-LDH, D-CoFeCu-LDH, D-NiCoCu-LDH, D-NiCoFe-LDH) using the same method. The SEM images (Figure 3) showed that the nanosheet morphology was retained across all samples, demonstrating that this defect engineering strategy was applicable to systems with different metal compositions. X-ray diffraction (XRD) patterns (Figure 1f) of all samples showed no distinct diffraction peaks corresponding to the typical LDH layered structure, likely due to the abundant defects and lattice distortions, which reduced long-range order. Diffraction peaks at 44.6°, 52°, and 76° corresponded to the nickel foam substrate (PDF#04-0850). Notably, in all copper-containing samples, characteristic diffraction peaks for metallic copper (Cu^0, PDF#04-0836) were observed, albeit with significant variations in intensity. We propose that, during electrodeposition, copper species preferentially deposit due to the high solubility product of copper hydroxide ($K_{sp} = 2.2 \times 10^{-20}$), potentially forming an intermediate copper oxide layer. Subsequently, based on copper's relatively positive reduction potential, some copper oxide may be reduced to Cu^0 nanoparticles during deposition or post-treatment [13]. Crucially, the Cu^0 diffraction peak in the multi-metal D-NiCoFeCu-LDH/NF is the weakest, suggesting that the strong synergistic effect among the metal elements in the high-entropy system effectively suppresses copper nanoparticle aggregation and growth, promoting the existence of copper species in the form of highly dispersed fine clusters. This structure is favorable for increasing the active interface and may regulate the electronic structure of the surrounding metal centers through electron effects.

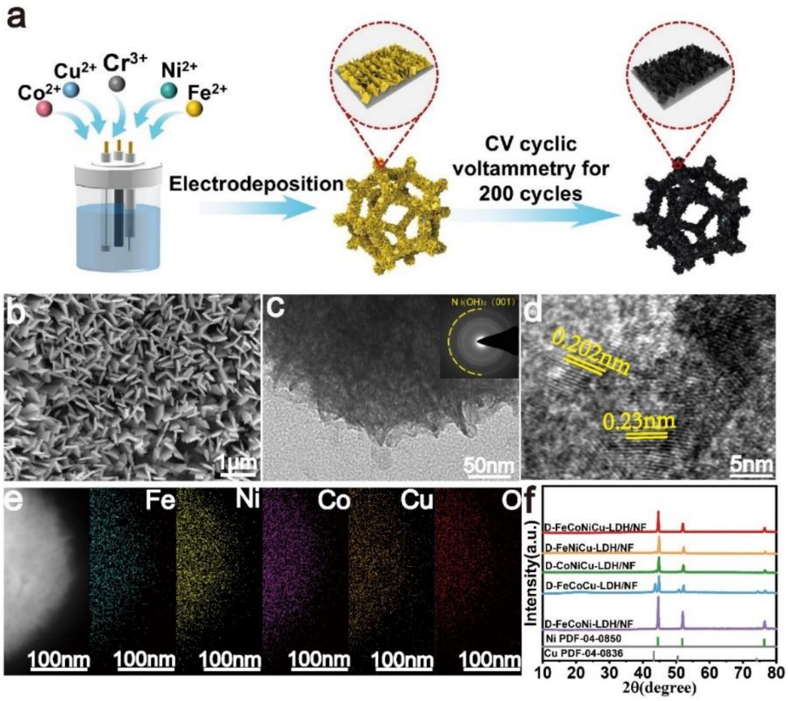

Figure 1. (a) Schematic of the synthesis process; (b) SEM image; (c) TEM image (inset: SAED pattern); (d) HRTEM image; (e) Elemental mapping; and (f) XRD pattern of D-NiCoFeCu-LDH.

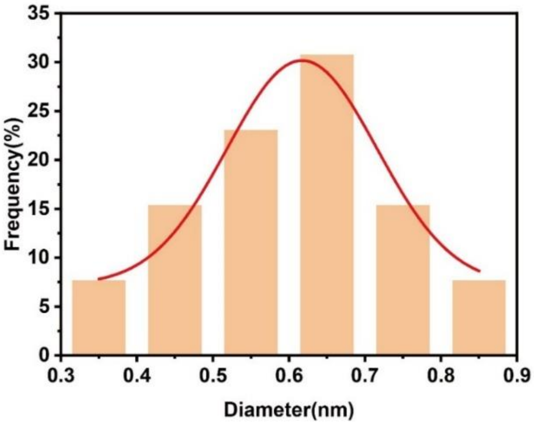

Figure 2. The size distribution curve of D-FeCoNiCu-LDH/NF.

Table 1. Comparison of elemental composition of catalysts determined by EDS.

Composition	Fe	Co	Ni	Cu	O
D-FeCoNiCu-LDH/NF	13	26	22	18	19
D-FeCoNi-LDH/NF	9	31	13	3	22

Table 2. Comparison of elemental composition of catalysts determined by ICP.

Composition	Fe	Co	Ni	Cu	Cr
D-FeCoNiCu-LDH/NF	16.13%	32.3%	27.3%	22.33%	1.6%

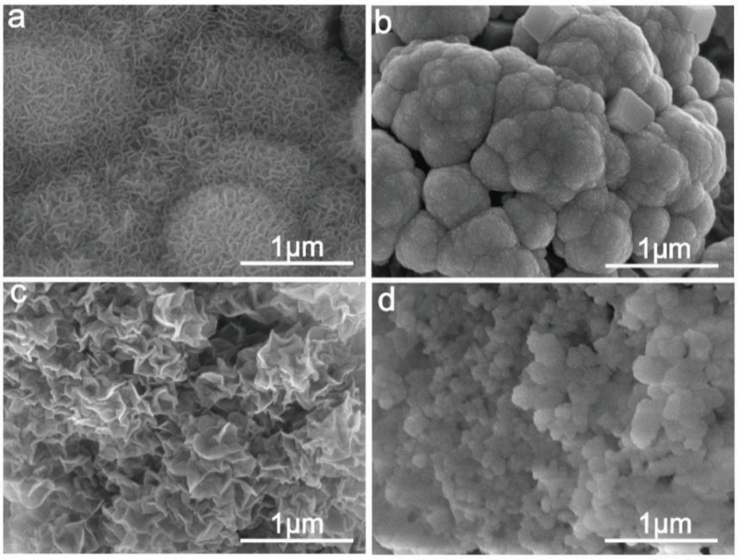

Figure 3. SEM images of (a) D-FeCoCu-LDH/NF; (b) D-FeNiCu-LDH/NF; (c) D-CoNiCu-LDH/NF; and (d) D-FeCoNi-LDH/NF.

3.2. Electrochemical performance

The OER performance of the synthesized catalysts was systematically evaluated in an O_2-saturated 1.0 M KOH electrolyte using a standard three-electrode system. LSV curves and corresponding overpotential bar charts (Figure 4a,b) reveal the decisive role of component synergism for catalytic activity. D-NiCoFeCu-LDH exhibits the best catalytic performance, requiring an overpotential of only 220 mV at a current density of 100 mA cm^{-2}, significantly lower than all the comparative samples. Compared to the precursor NiCoFeCuCr-LDH/NF (η_{100} = 290 mV), D-NiCoFeCu-LDH displays a 70 mV reduction in overpotential, providing strong evidence that selective chromium leaching via CV successfully introduces abundant defects, which serve as high-activity sites, significantly enhancing the intrinsic catalytic activity of the material. Additionally, systematic comparisons with the four-metal defect materials (D-NiFeCu-LDH, D-CoFeCu-LDH, D-NiCoCu-LDH, D-NiCoFe-LDH) enables the dissection of the synergistic roles of individual metal elements (Table 3). The absence of cobalt, nickel, or iron in any of the systems leads to a decrease in activity, with corresponding increases in overpotential by 47 mV, 74 mV, and 39 mV, respectively, indicating the crucial role these elements play in enhancing catalytic activity. Notably, D-NiCoFe-LDH, which lacks copper, exhibits the most significant performance degradation (η_{100} = 300 mV), emphasizing the central role of copper in modulating the overall electronic structure and reaction kinetics.

To investigate the cause of the observed activity differences, we assessed the electrochemical surface area (ECSA) of the materials by measuring double-layer capacitance (C_{dl}). As shown in Figure 5, D-NiCoFeCu-LDH exhibited the highest C_{dl} value (11 mF cm^{-2}), indicating that it exposed the most surface-active sites. Reaction kinetics were further analyzed using Tafel slopes and EIS [14,15]. As shown in Figure 4c, D-NiCoFeCu-LDH exhibited the lowest Tafel slope (19 mV dec^{-1}), indicating the most favorable reaction kinetics. This finding is consistent with EIS results (Figure 4d), where D-NiCoFeCu-LDH displayed the smallest charge transfer resistance (R_{ct} = 0.045 Ω), confirming that it facilitates faster electron transfer processes at the interface. These excellent charge transport properties are attributed to the unique electronic structure of the high-entropy material, where the uniform dispersion of multi-metallic elements and the rich defects synergistically optimize charge conduction in the bulk and surface phases. We compared the performance of D-NiCoFeCu-LDH with reported advanced transition metal-based catalysts (Figure 4e, Table 4). D-NiCoFeCu-LDH demonstrated remarkable advantages, in terms of the overpotential required to reach the same current density and the Tafel slope, highlighting its competitiveness. Long-term operational stability is a critical metric for evaluating catalyst practicality. As shown in Figure 4f, D-NiCoFeCu-LDH/NF maintained its stability after 500 hours of continuous testing at a high current density of 500 mA cm^{-2}, with only a 25 mV decrease in the operating potential and a stable chronopotentiometric curve. Furthermore, the LSV curves measured before and after the long-term stability test are nearly overlapped for D-NiCoFeCu-LDH/NF, further verifying its excellent structural and electrochemical robustness. In sharp contrast, D-FeCoNi-LDH sustains only 60 h at the same high current density of 500 mA cm^{-2}, accompanied by a remarkable potential increase of 250 mV, demonstrating its inferior long-term durability compared with D-NiCoFeCu-LDH/NF. Figure 6 presents the comparative characterizations of morphology, crystal structure, and surface electronic states of the defect-rich high-entropy D-NiCoFeCu-LDH catalyst before and after the 500-hour long-term oxygen evolution reaction stability test. After prolonged electrolysis, the morphology, composition, and surface structure of D-NiCoFeCu-LDH/NF have not shown apparent changes (Figure 6a–f) [16]. The above results verify that the D-NiCoFeCu-LDH/NF show an excellent OER stability.

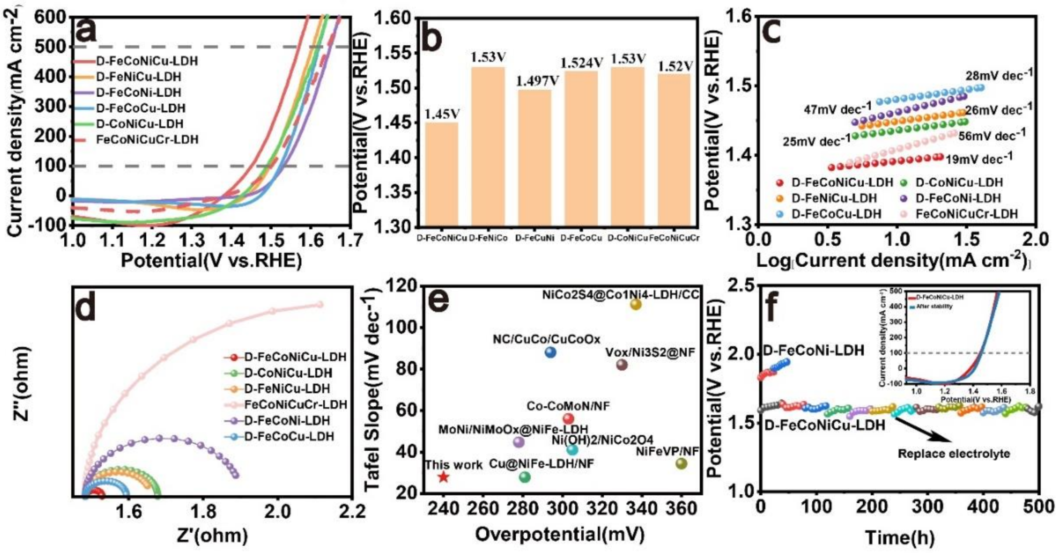

Figure 4. (a) LSV curves with iR compensation for different electrodes; (b) potential at j = 100 mA cm^{-2}; (c) Tafel slopes; (d) electrochemical impedance spectra; (e) comparison with literature at 100 mA cm^{-2}; and (f) chronopotentiometry of D-NiCoFeCu-LDH at 500 mA cm^{-2} for 500 h.

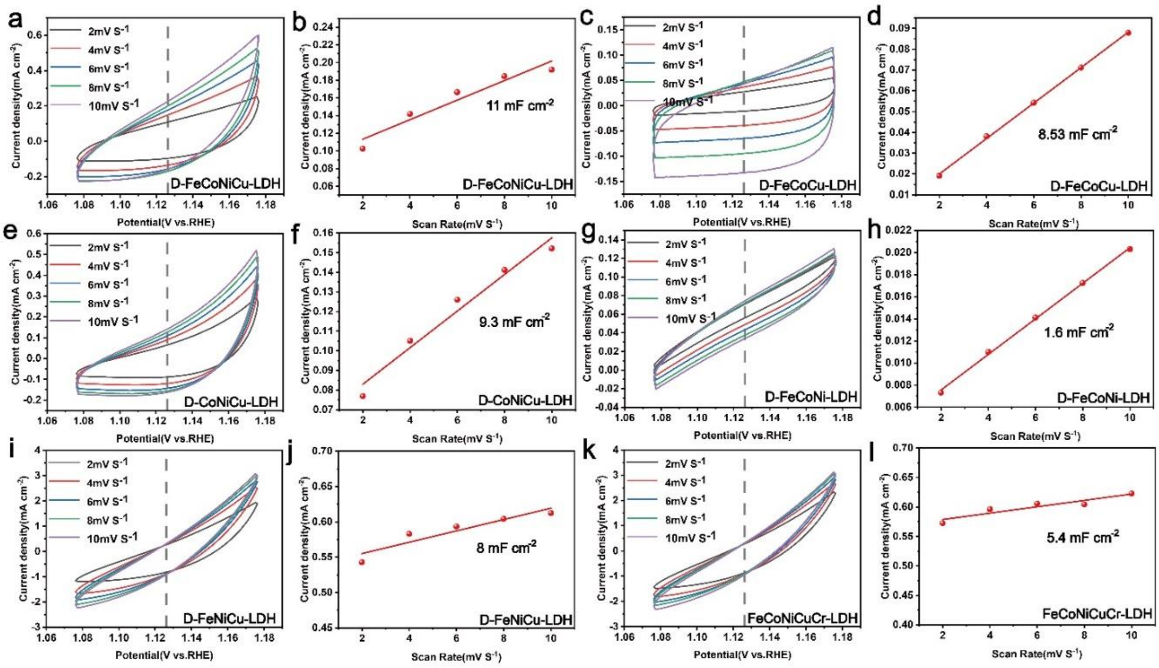

Figure 5. (a) CV curves at different scan rates in the non-Faradaic region; (b) capacitive currents on the basis of scan rates.

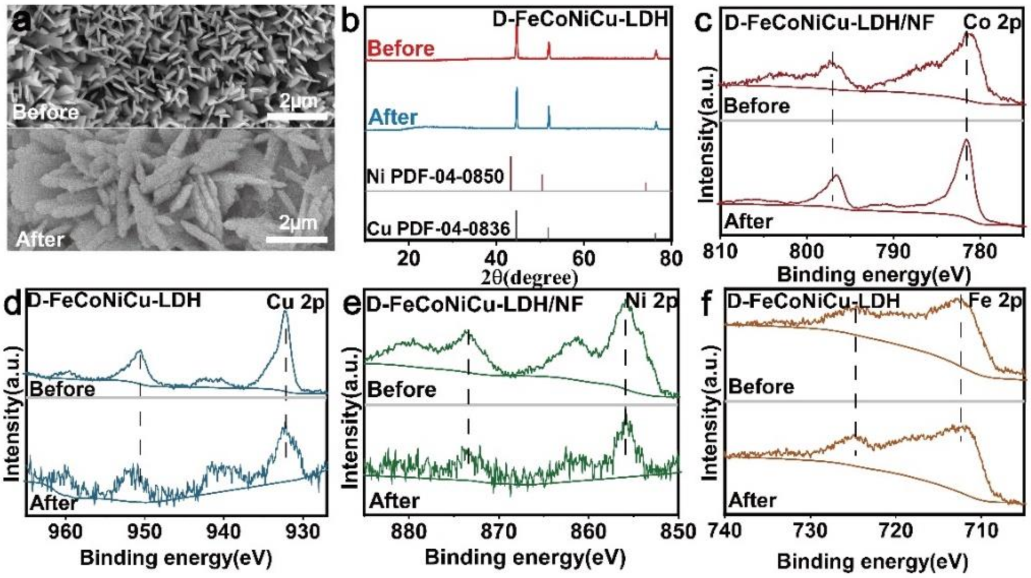

Figure 6. SEM images of D-FeCoNiCu-LDH: (a) before and after stability test; (b) XRD pattern, and XPS spectra; (c) Co 2p; (d) Cu 2p; (e) Ni 2p; and (f) Fe 2p for D-NiCoFeCu-LDH before and after the long-term stability test.

Table 3. Electrochemical performance of all sample.

Sample	η_{100} (mV)	C_{dl} (mF cm^{-2})	Tafel (mV dec^{-1})
D-FeCoNiCu-LDH/NF	220	11	19
D-FeCoNi-LDH/NF	300	1.61	47
D-FeCoCu-LDH/NF	294	8.53	28
D-FeNiCu-LDH/NF	267	8.03	26
D-CoNiCu-LDH/NF	259	9.32	25
FeCoNiCuCr-LDH/NF	290	5.42	56

Table 4. Performance comparison of different samples.

Sample	η_{100} (mV)	Tafel（mV dec^{-1}）	References
D-FeCoNiCu-LDH/NF	240	27.9	This work
Co-CoMoN/NF	303	56	[17]
NiFeVP/NF	360	34.4	[18]
NC/CuCo/CuCoOx	294	88	[19]
Cu@NiFe-LDH/NF	281	27.8	[20]
MoNi/NiMoOx@NiFe-LDH	278	44.7	[21]
NiCo2S4@Co1Ni4-LDH/CC	337	111.2	[22]
Ni(OH)2/NiCo2O4	305	41	[23]
Vox/Ni3S2@NF	330	82	[24]
Ir^{VI}-ado	1000	-	[25]

3.3. Mechanism

To gain deeper insights into the micro-mechanisms behind the enhanced performance of D-NiCoFeCu-LDH, we performed XPS analysis to compare the surface chemical states and electronic structures of D-NiCoFeCu-LDH and its key comparative sample, D-NiCoFe-LDH (Figures 7 and 8). The full spectra (Figure 7) confirmed the successful incorporation of copper, with elemental compositions consistent with the EDS results. Fine analysis of the high-resolution spectra revealed significant electronic redistribution effects triggered by Cu doping and defect engineering. The Cu 2p spectrum (Figure 8a) showed that the Cu $2p_{3/2}$ peak of D-NiCoFeCu-LDH can be deconvoluted into two major peaks at 932.57 eV and 952.36 eV, corresponding to Cu^+ and Cu^{2+} [26]. This result, in conjunction with the weak Cu^0 diffraction peak in the XRD pattern, suggests the presence of highly dispersed metastable Cu^0 cores within the material, while the surface is fully oxidized to stable Cu^+/Cu^{2+} species under ambient exposure and electrochemical testing conditions. These surface copper species are critical in inducing electronic structure modulation. More importantly, systematic shifts were observed in the electronic states of the Ni, Co, and Fe active centers. As shown in Figure 8b, the Ni 2p spectrum of D-NiCoFeCu-LDH exhibited a significantly enhanced Ni^{3+} contribution compared with D-NiCoFe-LDH, accompanied by a positive shift of approximately 0.44 eV in binding energy [27]. Similarly, the Co 2p (Figure 8c) and Fe 2p (Figure 8d) spectra display clear positive shifts of approximately 0.6 eV and 0.4 eV, respectively [28]. The simultaneous upward shift in binding energy for all primary metal species (Ni, Co, and Fe) indicates an overall increase in their average oxidation states and a decrease in local electron density [29]. Detailed deconvolution parameters and peak positions are summarized in Table 5. In the O 1s spectrum (Figure 8e), the metal–oxygen (M–O) lattice oxygen peak in D-NiCoFeCu-LDH also shifted toward higher binding energy relative to D-NiCoFe-LDH, suggesting reduced electron density on lattice oxygen species, consistent with the electron-deficient state of the metal centers [30]. These collective observations demonstrate a pronounced electronic redistribution induced by copper incorporation and the defect-rich high-entropy environment. The oxygen vacancy defects in the materials were quantitatively evaluated using EPR spectroscopy. As shown in Figure 8f, all samples exhibited a characteristic signal at $g \approx 2.003$. Notably, D-NiCoFeCu-LDH/NF exhibited the strongest EPR signal, significantly higher than that of its precursor NiCoFeCuCr-LDH/NF, while D-NiCoFe-LDH/NF displayed the weakest signal. This trend confirms that selective chromium leaching via cyclic voltammetry successfully introduces more oxygen vacancies, and in the high-entropy system, particularly with copper incorporation, oxygen vacancies are more easily formed and stabilized. The EPR results, in conjunction with the electron-deficient states observed at the metal sites in the XPS analysis, reveal a strong correlation between defects and electronic structure in D-NiCoFeCu-LDH/NF.

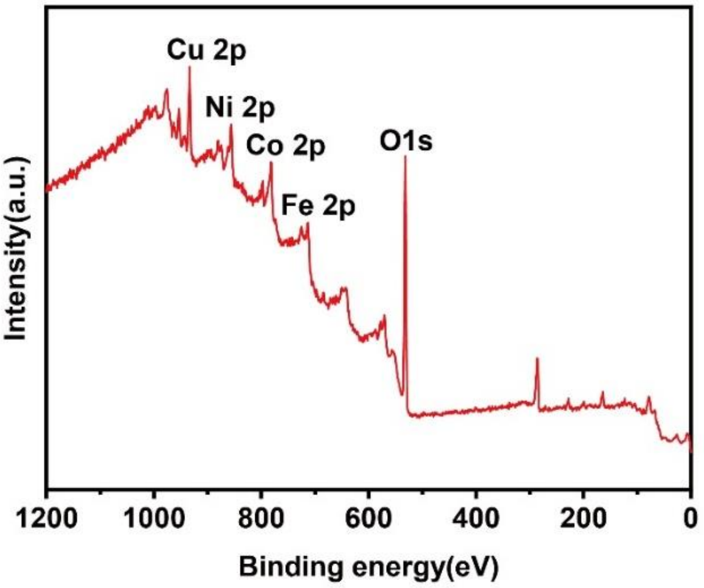

Figure 7. XPS spectra of D-FeCoNiCu-LDH/NF.

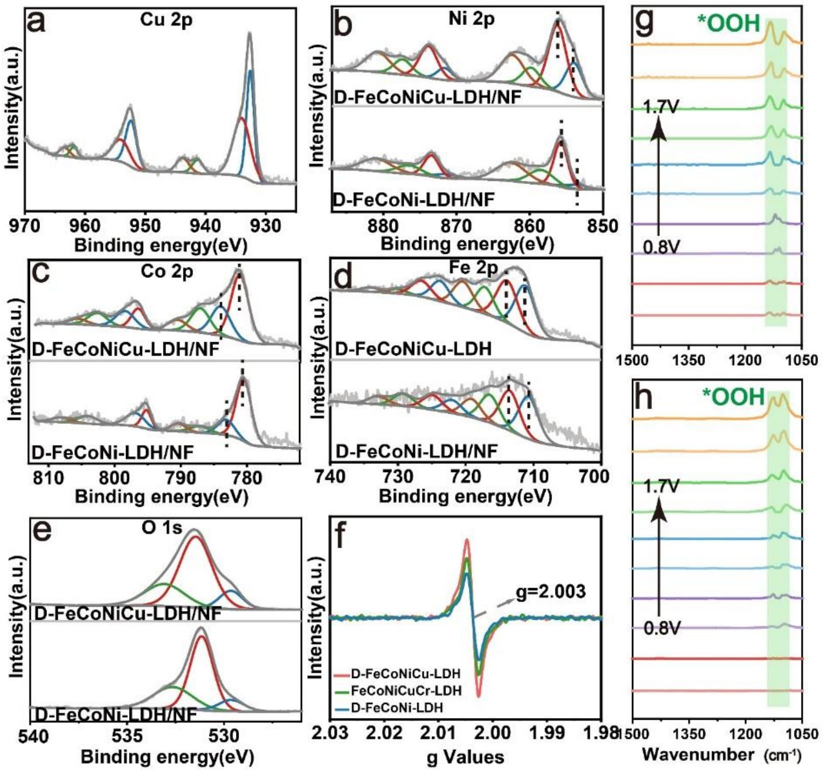

Figure 8. High-resolution XPS spectra of (a) Cu 2p, (b) Ni 2p, (c) Co 2p, (d) Fe 2p, and (e) O 1s for D-NiCoFeCu-LDH and D-NiCoFe-LDH; and (g-h) in situ ATR-SEIRAS during OER.

Table 5. XPS binding energy data for different elements in each sample.

Element		Einding Energy(eV)	
		D-FeCoNiCu-LDH/NF	D-FeCoNi-LDH/NF
Fe	Fe^{2+} 2p1/2	723.79	722.03
	Fe^{2+} 2p3/2	711.26	710.73
	Fe^{3+} 2p1/2	726.56	724.89
	Fe^{3+} 2p3/2	713.91	713.51
Co	Co^{2+} 2p1/2	798.43	796.87
	Co^{2+} 2p3/2	783.96	783.13
	Co^{3+} 2p1/2	796.44	780.46
	Co^{3+} 2p3/2	781.06	795.18
Ni	Ni^{2+} 2p1/2	871.62	873.00
	Ni^{2+} 2p3/2	853.97	855.70
	Ni^{3+} 2p1/2	873.83	875.08
	Ni^{3+} 2p3/2	856.20	855.16
Cu	Cu^{+} 2p1/2	952.36	
	Cu^{+} 2p3/2	932.57	
	Cu^{2+} 2p1/2	954.05	
	Cu^{2+} 2p3/2	933.99	
O		529.64	529.62
		531.45	531.15
		533.08	532.65

To elucidate the molecular-level mechanism behind the enhanced performance of D-NiCoFeCu-LDH, we employed in situ ATR-SEIRAS for the study. As shown in Figure 8g–h, during anodic scanning, a significant absorption band appeared in the 1050–1150 cm^{-1} region for D-NiCoFeCu-LDH/NF, corresponding to the O─O stretching vibration of surface-adsorbed superoxide species (*OOH) [31]. This indicates that its OER follows an adsorbate evolution mechanism (AEM). Compared to D-NiCoFe-LDH/NF, the characteristic peak for D-NiCoFeCu-LDH/NF appeared at a lower overpotential, with a significantly higher intensity at the same potential. This result suggests that the introduction of Cu significantly facilitates the conversion from *O to *OOH, thereby effectively lowering the kinetic barrier of the OER process. This is consistent with the lower Tafel slope observed in the electrochemical tests, further confirming the superior performance of this catalyst.

The highly dispersed Cu^{+}/Cu^{2+} species act as electronic modulators, and their relatively high electronegativity and variable oxidation states enable them to withdraw electron density from neighboring Ni, Co, and Fe sites through interfacial interactions, lowering the electron density at these metal centers [32]. The high-entropy structure and defects (such as oxygen vacancies) induce lattice strain and modify metal–oxygen bonding characteristics, further promoting electronic reconfiguration [33]. This optimized electronic structure increases the proportion of high-valence Ni^{3+}/Co^{3+} species, lowers the thermodynamic barrier for active phase transformation, and tunes the adsorption strength of key intermediates (*OH, *O, *OOH), thereby balancing the reaction free energy. Notably, it alleviates the energy barrier for the *O to *OOH conversion step [34], significantly enhancing the OER catalytic activity.

4. Conclusions

In summary, a defect-rich multi-metal high-entropy LDH (D-NiCoFeCu-LDH) was constructed via an "electrodeposition–electrochemical etching" strategy, yielding a 3D porous nanosheet array with uniform elemental distribution and abundant lattice defects. Electrochemical tests show excellent OER activity and long-term stability in alkaline media. Spectroscopic and comparative analyses reveal that highly dispersed Cu species synergize with the defect-rich high-entropy matrix to modulate Ni, Co, and Fe electronic structures, increasing oxidation states and optimizing intermediate adsorption. This enhances intrinsic catalytic activity and accelerates reaction kinetics. The work provides a rational strategy for designing high-performance, durable OER catalysts through multi-element synergy, and defect engineering.

Use of AI tools declaration

The authors declare they have not used Artificial Intelligence (AI) tools in the creation of this article.

Acknowledgments

This work was supported by the National Natural Science Foundation of China (Nos. 22109077) and the Natural Science Foundation of Shandong Province, China (ZR2021QB190).

Conflict of interest

The authors declare no conflicts of interest.

Author contributions

Chengshuo Du conducted the experiments, analyzed the data, and wrote the original draft. Shuxing Bai supervised the project, acquired funding, and reviewed the manuscript. Mingrui Guo conceptualized the study, provided methodological guidance, supervised the investigation, and revised the manuscript critically for important intellectual content. All authors have approved the final version of the manuscript.

References

1. Hoang AL, Balakrishnan S, Hodges A, et al. (2023) High-performing catalysts for energy-efficient commercial alkaline water electrolysis. *Sustainable Energy Fuels* 7: 31–60. https://doi.org/10.1039/d2se01197b
2. Tuysuz H (2024) Alkaline water electrolysis for green hydrogen production. *Acc Chem Res* 57: 558–567. https://doi.org/10.1021/acs.accounts.3c00709
3. Wang W, Yang B, Zhang H, et al. (2025) Novel synthesis of amorphous/defect-rich NiFe(O)OH nanosheets for alkaline electrolyzers at high current density. *Next Mater* 9: 101232. https://doi.org/10.1016/j.nxmate.2025.101232

4. Jia H, Yao N, Zhu J, et al. (2023) Reconstructured electrocatalysts during oxygen evolution reaction under alkaline electrolytes. *Chemistry* 29: e202203073. https://doi.org/10.1002/chem.202203073
5. Park H, Park BH, Choi J, et al. (2020) Enhanced electrochemical properties and OER performances by Cu substitution in $NiCo_2O_4$ spinel structure. *Nanomaterials (Basel)* 10: 1727. https://doi.org/10.3390/nano10091727
6. Bai J, Chen C, Lian Y, et al. (2024) Role of amorphous engineering and cerium doping in NiFe oxyhydroxide for electrocatalytic water oxidation. *J Colloid Interface Sci* 663: 280–286. https://doi.org/10.1016/j.jcis.2024.02.093
7. Li J, Wei Y, Zou L, et al. (2025) Cu dual-site doping: synergistic enhancement of OER activity through LDH and nickel foam interface engineering. *New J Chem* 49: 17577–17587. https://doi.org/10.1039/d5nj03068d
8. Sharma L, Katiyar NK, Parui A, et al. (2021) Low-cost high entropy alloy (HEA) for high-efficiency oxygen evolution reaction (OER). *Nano Res* 15: 4799–4806. https://doi.org/10.1007/s12274-021-3802-4
9. Ma Y, Ma Y, Wang Q, et al. (2021) High-entropy energy materials: Challenges and new opportunities. *Energy Environ Sci* 14: 2883–2905. https://doi.org/10.1039/d1ee00505g
10. Tomboc GM, Zhang X, Choi S, et al. (2022) Stabilization, characterization, and electrochemical applications of high-entropy oxides: Critical assessment of crystal phase–properties relationship. *Adv Funct Mater* 32: 2205142. https://doi.org/10.1002/adfm.202205142
11. Liang J, Cao G, Zeng M, et al. (2024) Controllable synthesis of high-entropy alloys. *Chem Soc Rev* 53: 6021–6041. https://doi.org/10.1039/d4cs00034j
12. Ding Y, Wang Z, Liang Z, et al. (2025) A monolayer high-hntropy layered hydroxide frame for efficient oxygen evolution reaction. *Adv Mater* 37: e2302860. https://doi.org/10.1002/adma.202302860
13. Jeung Y, Jung H, Kim D, et al. (2021) 2D-structured V-doped Ni(Co, Fe) phosphides with enhanced charge transfer and reactive sites for highly efficient overall water splitting electrocatalysts. *J Mater Chem A* 9: 12203–12213. https://doi.org/10.1039/d1ta02149d
14. Yan Y, Li P, Zhang Z, et al. (2024) Interfacial Si–O coordination for inhibiting the graphite phase enables superior SiC/Nb heterostructure joining by AuNi. *Composites Part B* 282: 111557. https://doi.org/10.1016/j.compositesb.2024.111557
15. Yang T, Yan Y, Liu R, et al. (2025) Engineering twins within lattice-matched Co/CoO heterostructure enables efficient hydrogen evolution reactions. *Nano Lett* 25: 7707–7715. https://doi.org/10.1021/acs.nanolett.5c00472
16. Wang R, Yang Y, Xu X, et al. (2023) Interface engineering and heterometal-doped FeOOH/Ga-Ni_3S_2nanosheet arrays for efficient electrocatalytic oxygen evolution. *Inorg Chem Front* 10: 1348–1356. https://doi.org/10.1039/d2qi02081e
17. Ma H, Chen Z, Wang Z, et al. (2022) Interface engineering of Co/CoMoN/NF heterostructures for high-performance electrochemical overall water splitting. *Adv Sci (Weinh)* 9: e2105313. https://doi.org/10.1002/advs.202105313
18. Hou J, Sun Y, Wu Y, et al. (2018) Promoting active sites in core–shell nanowire array as mott–schottky electrocatalysts for efficient and stable overall water splitting. *Adv Funct Mater* 28: 1704447. https://doi.org/10.1002/adfm.201704447

19. Yu L, Zhou H, Sun J, et al. (2017) Cu nanowires shelled with NiFe layered double hydroxide nanosheets as bifunctional electrocatalysts for overall water splitting. *Energy Environ Sci* 10: 1820–1827. https://doi.org/10.1039/c7ee01571b
20. Wu Y, Xu L, Xin W, et al. (2021) Rational construction of 3D MoNi/NiMoOx@NiFe LDH with rapid electron transfer for efficient overall water splitting. *Electrochim Acta* 369: 137680. https://doi.org/10.1016/j.electacta.2020.137680
21. Sang Y, Cao X, Wang L, et al. (2020) Facile synthesis of three-dimensional spherical $Ni(OH)_2/NiCo_2O_4$ heterojunctions as efficient bifunctional electrocatalysts for water splitting. *Int J Hydrogen Energy* 45: 30601–30610. https://doi.org/10.1016/j.ijhydene.2020.08.097
22. Yuan F, Wei J, Qin G, et al. (2020) Carbon cloth supported hierarchical core-shell $NiCo_2S_4$@CoNi-LDH nanoarrays as catalysts for efficient oxygen evolution reaction in alkaline solution. *J Alloys Compd* 830: 154658. https://doi.org/10.1016/j.jallcom.2020.154658
23. Niu Y, Li W, Wu X, et al. (2019) Amorphous nickel sulfide nanosheets with embedded vanadium oxide nanocrystals on nickel foam for efficient electrochemical water oxidation. *J Mater Chem A* 7: 10534–10542. https://doi.org/10.1039/c8ta12483c
24. Huo M, Liang Y, Qin K, et al. (2024) Hexavalent iridium boosts oxygen evolution performance. *Green Carbon* 2: 403–404. https://doi.org/10.1016/j.greenca.2024.07.003
25. Shu W, Sun Q, Huang K, et al. (2024) V-Doping induced surface electron modulation and nanostructure design for $Ni(OH)_2$/GO towards efficient urea electro-oxidation. *Chem Commun (Camb)* 60: 13267–13270. https://doi.org/10.1039/d4cc04157g
26. Zhang L, Cai W, Bao N (2021) Top-level design strategy to construct an advanced high-entropy Co-Cu-Fe-Mo (oxy)hydroxide electrocatalyst for the oxygen evolution reaction. *Adv Mater* 33: e2100745. https://doi.org/10.1002/adma.202100745
27. Zhang W, He X, Pan P, et al. (2025) Cr-enhanced selective dealloying and sequential electrochemical reconstruction to tailor NiFe-based integrated catalysts for industrial-level water oxidation. *Energy Environ Sci* 18: 8697–8707. https://doi.org/10.1039/d5ee03448e
28. Wang L, Gao Z, Su K, et al. (2024) Stacked high-entropy hydroxides promote charge transfer kinetics for photoelectrochemical water splitting. *Adv Funct Mater* 34: 2403948. https://doi.org/10.1002/adfm.202403948
29. Zhong X, Wang HY, Zhang C, et al. (2025) High-valence metal modulating lattice oxygen in high-entropy layered double hydroxides for enhanced oxygen evolution reaction. *Adv Funct Mater* 35: e18240. https://doi.org/10.1002/adfm.202518240
30. Li X, Wang J, Xue H, et al. (2025) Tuning α-MnOOH formation via atomic-level Fe introduction for superior OER performance. *Adv Funct Mater* 35: 2503360. https://doi.org/10.1002/adfm.202503360
31. Chang R, Pang Y, Yang Q, et al. (2025) High entropy hydroxide with a hollow nanocage structure promotes efficient and stable water/seawater electro-oxidation. *Chem Sci* 16: 11961–11969. https://doi.org/10.1039/d5sc01961c
32. Wang F, Feng L, Zhang M, et al. (2025) Engineering oxygen nonbonding states in high entropy hydroxides for scalable water oxidation. *Nat Commun* 16: 6624. https://doi.org/10.1038/s41467-025-61766-2
33. Yang H, Li F, Zhan S, et al. (2026) Metal-hydroxyls mediate intramolecular proton transfer in heterogeneous O-O bond formation. *Nat Chem* 18: 335–344. https://doi.org/10.1038/s41557-025-01993-8

34. Zhang Y, Zheng T, Dai H, et al. (2025) Lattice oxygen-mediated water oxidation on reconstructed Ni_3S_2/NiFeOOH heterointerfaces. *Chemistry*, e03063. https://doi.org/10.1002/chem.202503063